Available online at www.sciencedirect.com

jmr&t Journal of Materials Research and Technology

journal homepage: www.elsevier.com/locate/jmrt

Original Article

Effect of the Ti/Ta ratio on the feasibility of porous Ti_{25+x}-Nb_{25}-Zr_{25}-Ta_{25-x} (X= 0, 5, and 10) alloys for biomedical applications

G. Al Hawajreh [a], G. Gonzalez [b,*], L. Romero-Resendiz [c,**], A. Vidilli [d], L.B. Otani [e], V. Amigó [a,***]

[a] Instituto de Tecnología de Materiales, Universitat Politècnica de València, Camino de Vera S/n, 46022, Valencia, Spain

[b] Instituto de Investigaciones en Materiales, Universidad Nacional Autónoma de México, Circuito Exterior S/N, Cd. Universitaria, A. P. 70-360, Coyoacán, C.P. 04510, Mexico

[c] Facultad de Química, Departamento de Ingeniería Metalúrgica, Universidad Nacional Autónoma de México, Mexico City, 04510, Mexico

[d] Federal University of Sao Carlos, Graduate Program in Materials Science and Engineering, Rod. Washington Luis, s/n-Monjolinho, Sao Carlos, SP, 13565-905, Brazil

[e] Universidade Federal de São Carlos, Department of Materials Engineering (DEMa), Rod. Washington Luis, km 235, São Carlos, SP, 13565-905, Brazil

ARTICLE INFO

Article history:
Received 2 March 2023
Accepted 9 April 2023
Available online 12 April 2023

Keywords:
Refractory high-entropy alloy
Mechanical properties
Ion release
Corrosion
Microstructure

ABSTRACT

Non-toxic biomedical HEAs by powder metallurgy methods have been scarcely studied despite their promising mechanical and biological behaviors. This work studied the microstructural, mechanical, electrochemical, and ion release effects of the Ti/Ta ratio on three porous Ti–Nb–Zr–Ta (TNZT) alloys. The microstructure of the TNZT alloys consisted of semi-equiaxed and micrometric BCC-phases (matrix) with lower contents of HCP phase. Elastic moduli (82–91 GPa), hardness (373–430 HVN), ultimate bending (225–475 MPa), and tensile (119–256 MPa) strength, electrochemical corrosion (4.5–9.6 μm $year^{-1}$), and ion release (toxicity, 0.9–1.1 μm $year^{-1}$) were within acceptable limits for implant biomaterials. Increasing the Ti content (and decreasing Ta) was advantageous for improving mechanical strengthening and reducing the elastic modulus. The medium value of elastic modulus may be beneficial to reduce the mechanical mismatch between the implant and the organic tissue. However, the corrosion rate and metallic ion release increased as a function of the Ti content. Besides, the alloy with the lowest Ti content (highest Ta content) showed local corrosion. Based on the above, the porous TNZT alloys with medium and highest Ti

* Corresponding author.
** Corresponding author.
*** Corresponding author.
E-mail addresses: joseggr@unam.mx (G. Gonzalez), liliana.rom7@comunidad.unam.mx (L. Romero-Resendiz), vamigo@mcm.upv.es (V. Amigó).

https://doi.org/10.1016/j.jmrt.2023.04.070

contents (30 and 35 wt%) were demonstrated as promising candidates for biomedical implant applications.

1. Introduction

The biomedical implants market is expected to increase with the worldwide population and aging [1,2]. Multiple biomedical implant materials are being studied to overcome this growing need. Hardness and strengthening equal to or higher than that of the human bone, biocompatibility, high corrosion resistance, and low elastic modulus are at the core of the required properties for successful implants [3,4]. Ti and its alloys are the most useful metallic implants due to their adequacy with those requirements. However, some common alloys, such as Ti–6Al–4V, contain alloying elements highly toxic to the human body [5].

Ti–Nb–Zr–Ta (TNZT) is an alloy system specially designed with non-toxic elements for biomedical implant applications. Moreover, Nb, Zr, and Ta stabilize the β-BCC-Ti phase, which is commonly sought due to its lower elastic moduli compared to α-HCP-Ti alloys [5,6]. Besides, the TNZT is a high-entropy alloy (HEA), i.e., different from traditional alloys based on a major alloying element, with equiatomic or near-equiatomic concentrations of at least four constituent elements [7]. In addition, the absence of long-range-order (LRO) in HEAs may influence the strength of its multi-atomic interatomic bonding. As different pairs of atoms may be found at similar separation distance in HEAs, many possible bond strength values can be found between them [8]. Thus, the elastic moduli of HEAs, which is highly dependent on the strength bonding, may vary from the classic alloys with a major element.

Furthermore, the high chemical disorder and the proximity to the solubility limit in HEAs also discourage the formation of secondary phases [7]. The lack of interfaces with high chemical differences in single-phase microstructures reduces the formation of galvanic pairs. Thus, single-phase HEAs may be advantageous in terms of low pitting probability. Due to the above, the TNZT and other HEAs have been reported as promising for biomedical implant applications [8,9]. However, the elastic modulus of human bone is still difficult to reach with dense alloys.

Functional porosity can reduce the elastic modulus of biomedical HEAs and other alloys [8,10], as well as encourage the anchorage of organic tissue to the implant [10–12]. Powder metallurgy (PM) methods have produced several porous biomedical Ti alloys [13–15]. Among the PM methods, press & sintering (P&S) is one of the most cost-effective [16], which is an important factor in biomedical implants.

Despite the abovementioned advantages, there is scarce information on biomedical HEAs produced by PM methods [17]. Besides, studying the effect of different alloying elements on the desired BCC phase is crucial for seeking adequate mechanical and electrochemical performance. Some efforts regarding the effect of O, Sn, Fe and Si in the mechanical and electrochemical properties of Ti–Ta and TNZT alloys have been done [18–21]. Nonetheless, the effect of the Ti/Ta ratio in porous TNZT alloys has not been well-studied. Else than non-toxic and biocompatible [22], tantalum has the same crystalline BCC-cell as the β-BCC-Ti phase, being a promising element for biomedical purposes.

This work aims to study the effect of the Ti/Ta ratio on the microstructure, mechanical, electrochemical, and ion release behavior of the TNZT system. The chemical composition, as well as the processing route, were selected to produce TNZT alloys that meet all the requirements for biomedical implants, i.e., hardness and strength equal to or higher than the human bone, high corrosion resistance, non-toxicity, biocompatibility, and medium elastic modulus. The elaboration route also followed the principles of low-cost processing and handling security by using non-pyrophoric raw powder elements. This work is expected to serve as a basis for future bio-HEAs designs.

2. Experimental procedure

2.1. *Elaboration of TNZT HEAs*

The chemical composition was selected based on CALPHAD method to promote nearly-BCC phase alloys. Thermodynamic phase equilibrium calculations were carried out using Thermo-Calc® (2022a) software and the TCHEA3 database. The temperature range studied was 200–2000 °C. The different elements for PM blend elements preparation are shown in Table 1, all of them were purchased from Alfa Aesar. The generic chemical formula of the elaborated HEAs is $Ti_{(25+x)}$-Nb_{25}-Zr_{25}-$Ta_{(25-x)}$, where X = 0, 5, 10 at.%. The HEAs were then identified as Ti_{25} (25Ti–25Nb–25Zr–25Ta), Ti_{30} (30Ti–25Nb–25Zr–20Ta), and Ti_{35} (35Ti–25Nb–25Zr–15Ta).

The powders were weighted to the chosen composition and mixed by a blender model Bioengineering Inversine 2L in a closed vial for 30 min at 54 rpm. Blend element was used before sintering to enhance the surface contact between elemental powders and secure their homogeneous mixing. Thus, it avoids excessive welding and limits particle growth. Approximately 8 g of powders were compacted at 1000 MPa through a rectangular die with dimensions 32 × 12 × 6 mm. The specimens were sintered in a high-vacuum tubular furnace (Carbolite HVT 15/75/450) at a pressure between 0.01

Table 1 – Characteristics of raw powders used to produce the HEAs.

Element	Powder size/μm	Purity/wt.%
Titanium	44	99.7
Niobium	5	99.8
Zirconium	44	99.7
Tantalum	5	99.8

and 0.1 Pa. A two-steps sintering process was performed as follows: 1) increasing temperature at a speed of 5 °C min^{-1} until 800 °C and maintaining for 2 h, and 2) increasing temperature up to 1400 °C and maintaining the temperature for 3 h. Ar atmosphere was applied during sintering to avoid oxidation. Posteriorly, the samples were furnace-cooled at 10 °C min^{-1}.

2.2. Microstructural characterization

Cross-sections of the HEAs were subjected to standard metallographic preparation, i.e., griding with SiC papers and polishing with an OP-S NonDry suspension of 0.04 μm particle size diluted in 20% H_2O_2. The analyses of phase content and lattice parameters were performed by X-ray diffraction (XRD, Bruker D2Phaser) with Cu Kα radiation (λ = 0.15418 nm) at 30 kV and 15 mA, step size of 0.02° and scanning speed of 0.0025° s^{-1}. Rietveld refinement was performed by MAUD software version 2.94 [23].

Porosity, phase, and grain distributions, and crystallographic texture were analyzed by electron backscatter diffraction (EBSD, Oxford Instruments Ltda.) coupled to a scanning electron microscope (SEM, ZEISS-ULTRA 55). Chemical microanalysis was applied by energy dispersive spectroscopy (EDS) using an Oxford Instruments X-ray detector installed in the SEM. NIS-Elements® image analysis software was used to quantify internal porosity and phases.

2.3. Mechanical properties evaluation

Microhardness was measured on the polished HEAs according to the ASTM: E384 using an HMV, Shimadzu Micro Hardness Tester at 0.98 N for 15 s. The elastic modulus was measured by impulse excitation technique (IET, ATCP-Sonelastic). The software ATCP Sonelastic 3.0 was used to analyze the data. Four-point bending tests were performed according to the ASTM: E855 on samples with a geometry of 30 × 12 × 5 mm. A Shimadzu universal testing machine model AG-100kN Xplus was used. The space between the down supports was 22 mm and the upper supports was 11 mm. For tensile tests, dog-bone-shape tensile specimens were sintered and polished up to a thickness of 0.9 mm. A gauge length of 9.40 mm and width of 1.75 mm were used. The tensile tests were performed according to the ASTM D3039. Five measurements per sample were taken from each mechanical test for statistical purposes.

2.4. Electrochemical evaluation

The corrosion study was carried out in samples polished up to mirror appearance and ultrasonically cleaned in a 50 vol% solution of acetone and alcohol. A potentiostat/galvanostat (Metrohm potentiostat- AUTOLAB AU51095 combined with NOVA software) was used on an exposed surface of 0.785 cm^2 using a three-electrode cell. Ag/AgCl and platinum electrodes were used as reference and auxiliary electrodes, respectively. The electrolyte consisted of a modified Ringer's-Hartmann's solution based on NaCl, KCl, $CaCl_2$, and sodium lactate, with a pH between 6 and 7.2 at 37 °C. Before measurements, the sample was cathodically cleaned by applying a potential of −1.15 V for 5 min. Cathodic cleaning avoided results being altered by the reduction of the oxide surface layer, which may be formed on the electrode surface. The open circuit potential (OCP) measurements were performed for 100 min. Potentiodynamic (PD) polarization curves were measured at a scan rate of 2 mV s^{-1} and potential range from −0.5 to 3.0 V. The corrosion parameters; corrosion current density (i_{corr}), polarization resistance (R_p), and corrosion rate (C_r), were determined by Tafel's extrapolation and Faraday's first law methods using Wolfram Mathematica 12.1 and Eqs. (1) and (2) [24],

$$R_p = \frac{\beta_a \beta_c}{2.303\, i_{corr}\,(\beta_a + \beta_c)} \quad (1)$$

$$C_r = K\,\frac{w\, i_{corr}}{\rho} \quad (2)$$

where β_a and β_c are the anodic and cathodic Tafel slopes obtained from the active region of the PD curves, the i_{corr} was obtained from the intersection between anodic and cathodic slopes, w is the equivalent weight, K is the Faraday's constant with value of 3.27 × 10^{-6} μm A^{-1} cm^{-1} $year^{-1}$, and ρ is the density of the alloys. The measured densities of the Ti_{25}, Ti_{30}, and Ti_{35} samples (8.913, 8.366, and 7.779 g cm^{-3}, respectively) were considered to estimate the corrosion rate. The corrosion potential (E_{corr}), which is the potential at which the oxidation rate equals the reduction rate, was directly obtained from the PD curves. Three samples per condition were studied.

2.5. Ion release

To evaluate cytotoxicity, ion release measurements were carried out in samples polished up to mirror appearance and sterilized. The size of the studied samples was 1.12 cm^2 and the contact surface was 0.744 cm^2. The samples were immersed in 50 mL of Ringer-Hartmann solution composed of NaCl (5.97 g L^{-1}), KCl (0.37 g L^{-1}), $CaCl_2$ (0.22 g L^{-1}) and $C_3H_5O_{3x}Na$ (3.25 g L^{-1}). The electrolyte was adjusted to a pH of 6.53, slightly lower than 7 to be similar to the average pH of the intra-oral environment [25]. The samples were kept at the average body core temperature, i.e., 37 °C [26], for 732 h. After incubation, the microstructural attack due to the corrosive environment was observed by optical and scanning electron microscopes. Inductively coupled plasma optical emission spectrometry (ICP-OES, Varian 715-S) was used to measure the concentrations of Ti, Zr, Nb, and Ta ions dissolved in the incubated medium. The used wavelengths were 336.1 nm (Ti), 316.3 nm (Nb), 343.8 nm (Zr), and 268.5 nm (Ta). Three repetitions of each sample were analyzed for statistical purposes.

3. Results

3.1. Thermodynamic phase equilibrium calculations

The temperature transformation of equilibrium phases based on the composition of the alloys was calculated and shown in Fig. 1. BCC1, BCC2, and HCP phases can be formed in the three studied compositions. BCC1 and BCC2 are two body-centered cubic phases composed by Ti, Nb, and Zr, Ta, each of these phases differ in their specific composition. HCP is a hexagonal

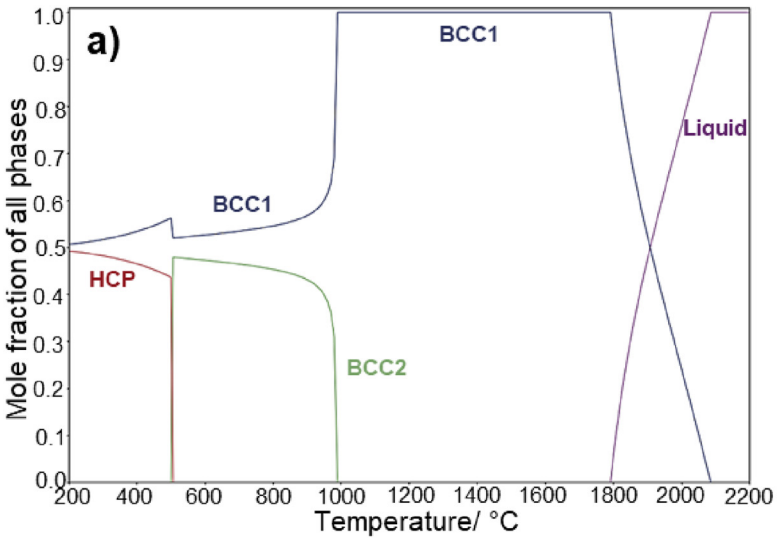

Temperature	Phase	Composition
600 °C	BCC1	$Ti_{12}Nb_{40}Zr_4Ta_{44}$
	BCC2	$Ti_{39}Nb_8Zr_{49}Ta_4$
300 °C	BCC1	$Ti_4Nb_{48}Ta_{48}$
	HCP	$Ti_{49}Zr_{51}$

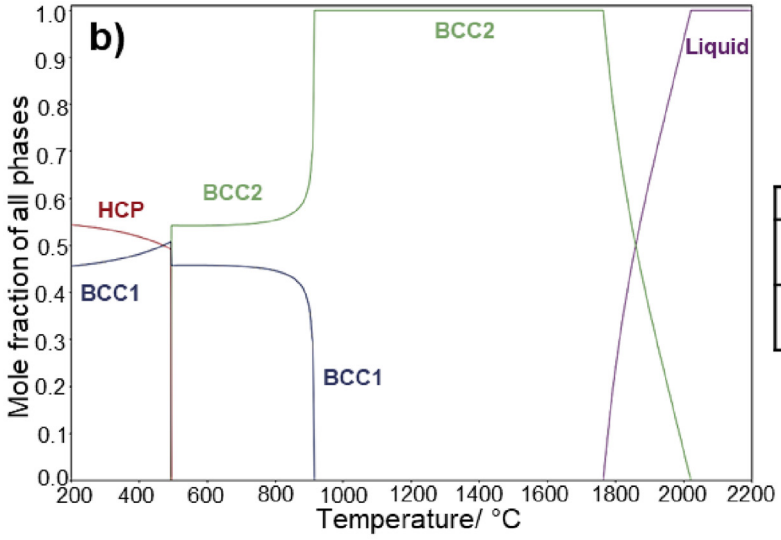

Temperature	Phase	Composition
600 °C	BCC1	$Ti_{14}Nb_{43}Zr_4Ta_{39}$
	BCC2	$Ti_{44}Nb_9Zr_{43}Ta_4$
300 °C	BCC1	$Ti_4Nb_{53}Ta_{43}$
	HCP	$Ti_{53}Zr_{47}$

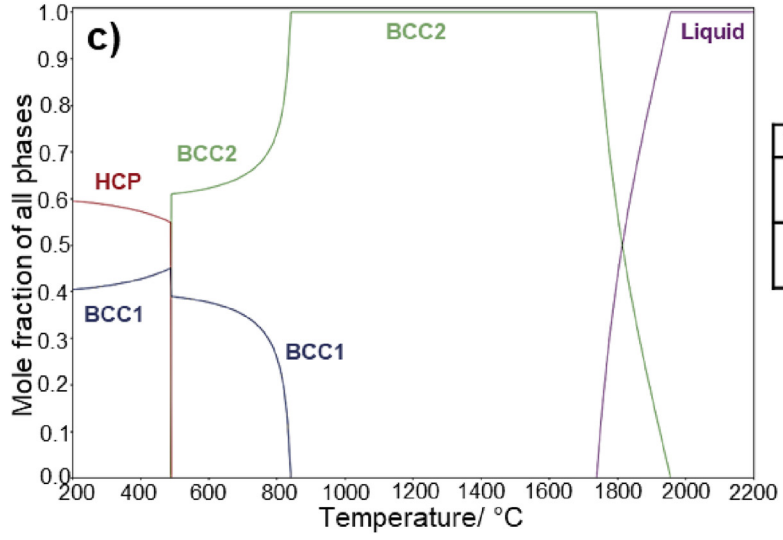

Temperature	Phase	Composition
600 °C	BCC1	$Ti_{15}Nb_{48}Zr_4Ta_{33}$
	BCC2	$Ti_{47}Nb_{11}Zr_{38}Ta_4$
300 °C	BCC1	$Ti_3Nb_{60}Ta_{37}$
	HCP	$Ti_{60}Zr_{40}$

Fig. 1 – Amount and composition of phases determined by thermodynamic equilibrium for the a) Ti_{25}, b) Ti_{30}, and c) Ti_{35} samples.

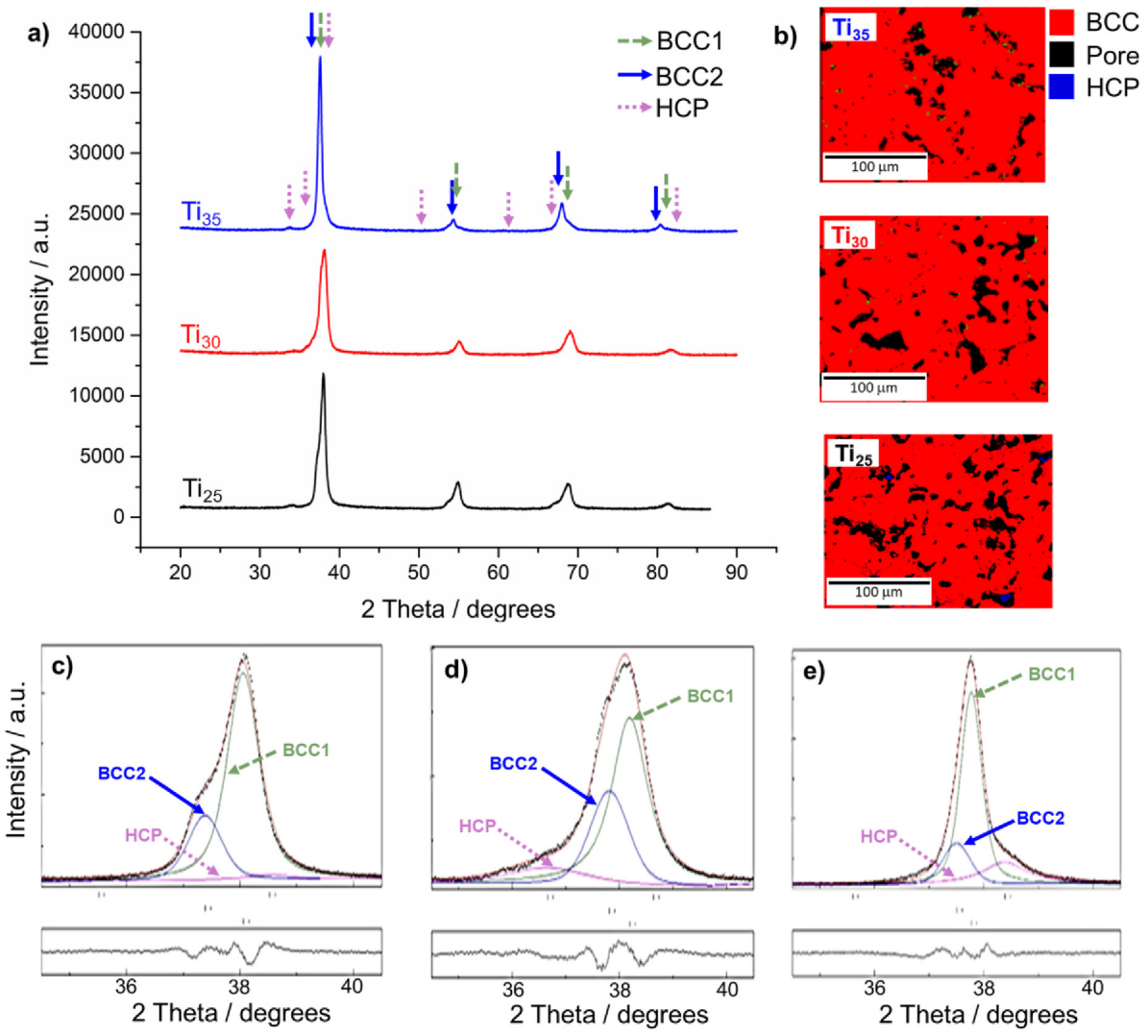

Fig. 2 – a) Diffractogram of the studied HEAs with b) EBSD phase mapping, and magnifications of the convoluted peaks of (110)-BCC1, (110)-BCC2, and (101)-HCP phases of c) Ti_{25}, d) Ti_{30}, and e) Ti_{35} samples after Rietveld refinement.

close-packed structure predicted by thermodynamical calculations, but in practice, the amount of this phase is negligible due to the low element diffusivity at low temperatures.

Regarding Ti25 composition simulation shown in Fig. 1a, the first formed solid phase has a BCC structure (T = 1790 °C), followed by a biphasic region BCC1 and BCC2 that starts at 990 °C. At temperatures lower than 500 °C, BCC1 remains stable but BCC2 decomposes forming an HCP phase. To follow the element segregation, the composition of the BCC1, BCC2, and HCP phases were calculated and shown as inserted tables next to each phase diagram in Fig. 1. At 600 °C, BCC1 is enriched in Ta and Nb whereas BCC2 is rich in Zr and Ti. At 300 °C, BCC1 is no longer a quaternary but a ternary phase, always rich in Nb and Ta, whereas HCP is a binary Ti–Zr phase.

For the Ti30 composition shown in Fig. 1b, solidification of a single-phase BCC microstructure starts at 1770 °C. The upper-temperature limit of the BCC1-BCC2 biphasic zone shifted to a lower temperature (920 °C) compared to that on the Ti25 sample. Although, the transformation from BCC2 to HCP remains at 500 °C. The atomic segregation is similar to that found for Ti25 sample. At 600 °C BCC1 and BCC2 are rich in Nb–Ta and Zr–Ti, respectively. Whereas, at 300 °C the stable phase BCC1 is rich in Nb–Ta and the HCP phase is a binary Ti–Zr phase. Finally, for the Ti35 composition shown in Fig. 1c, the solidification path is quite similar to that of the Ti30 sample, and the predominant elements in the phases BCC1, BCC2, and HCP are the same.

Similar heterogeneous elemental distribution has been reported in Ti–Nb and Ti–Ta alloys produced by spark plasma sintering (SPS) [27,28]. Where Ti- and Nb-rich regions were obtained in the sintered samples without homogenization heat treatments. The heterogeneous elemental distribution is related to the low diffusion of Ta, Nb, and Zr in β-Ti and the low diffusion between Ta and Ti during sintering [27–29].

Table 2 – Lattice parameters and phases content calculated from Rietveld refinement on the Ti_{25}, Ti_{30}, and Ti_{35} samples.

Sample	Lattice parameter/Å	Relative abundance/wt.%	Rs factors
Ti_{25} (x = 0)	BBC1, a = 3.3410	69	Rwp 4.17
	BCC2, a = 3.3988	23	Rb 3.33
	HCP, a = 3.0405 c = 5.0514	8	Rexp 3.14
Ti_{30} (x = 5)	BCC1, a = 3.3295	59	Rwp 4.37
	BBC2, a = 3.3616	37	Rb 3.47
	HCP, a = 3.0559 c = 4.8980	4	Rexp 3.13
Ti_{35} (x = 10)	BCC1, a = 3.3651	57	Rwp 4.91
	BCC2, a = 3.3882	36	Rb 3.70
	HCP, a = 3.0558 c = 5.0391	7	Rexp 3.17

3.2. *Microstructural characterization*

Fig. 2a shows the XRD patterns of Ti25, Ti30, and Ti35 samples. The diffractograms showed two different BCC phases, BCC1 and BCC2, and an HCP phase. The EBSD phase mappings, inserted in Fig. 2b show the dominant presence of BCC phases (red-colored zones in at least 98%). Minor regions were indexed as hexagonal phase (blue color) visible only for Ti25. Fig. 2c–d shows the deconvoluted contributions of BCC1, BCC2, and HCP at 38° according to the Rietveld refinement. It is worth noting that peak width changes appreciably, denoting that the BCC1/BCC2 relative amount differs depending of Ti and Ta amount. On other hand, HCP peak phase is completely overlap at this position but is unambiguously determined with the peak (100) located around 34°.

The lattice parameters and relative abundance determined by Rietveld refinement are indicated in Table 2. The three studied samples are mainly composed of BCC1 phase. The lattice parameters of the BCC1 phase (3.32–3.36 Å) are nearly similar to the theoretical lattice parameter (3.31 Å at 900 °C) of the chemically pure BCC-β-Ti phase [30].

The changes in lattice parameters between the BCC1 and BCC2 phases could be explained in terms of their chemical differences. According to the thermodynamic calculation shown in Fig. 1, BCC1 is rich in Nb–Ta, whereas BCC2 is rich in Ti–Zr. Nevertheless, experimentally, it is difficult to directly correlate the elemental distribution by EDS and the composition of BCC1 and BCC2. Besides, an incomplete reaction between raw powder cannot be discarded. Fig. 3 shows element segregation observed by EDS. The Ti, Nb, Zr, and Ta mappings clearly show the element segregation, predicted qualitatively by the thermodynamic simulation.

Fig. 4 shows the EBSD mapping based on inverse pole figures (IPF) contrast. Despite the grain morphology being nearly equiaxial in the three Ti25, Ti30, and Ti35 samples, the grain average diameter increased from 35, 65, to 90 μm, respectively. If we compare this microstructure with the phases obtained by XRD, it is observed that the larger amount in Ti, also produced an almost single single-phase system, both effects could be related due to the grain growth is favored if one single phase exists (BCC1). In other words, without the presence of a second phase (BCC2) or its associated interfaces, grain boundaries can move more freely, allowing grains to grow in size.

Despite the grain misorientation distribution has no high accuracy due to the reduced sampling (micrometric grain sizes), the three analyzed samples showed an arbitrary grain orientation distribution. The random crystallographic orientation can be observed from the comparison between the theoretical distribution for randomly-oriented cubic polycrystals [31] and the uncorrelated (random pair distribution) misorientation distribution. From Fig. 4b,d,f, the theoretical and the uncorrelated distributions evidenced nearly similar profiles. The high relative frequency at misorientation angles <2° may be related to the probability of random points falling on the same grain, which may be high in the coarse-grained microstructures of Fig. 4.

3.3. *Mechanical properties evaluation*

Fig. 5 shows bending and tensile test plots for the Ti_{25}, Ti_{30}, and Ti_{35} samples. As TNZT alloys are composed of non-toxic elements, they are expected to have broad uses for biomedical implants, including dental and body prostheses. Thus, bending and tensile are common stress states induced during chewing, flexion of articulations, and support of human weight in reduced areas (such as the knees), among others.

As a general trend, the ultimate strength (US) by both techniques showed an increment as a function of the Ta decrement (Ti increment). However, elongation does not show a trend with the increment of Ti by remaining similar in tensile test but increasing in bending tests. From tensile test (Fig. 5b), none of the studied Ti_{25}, Ti_{30}, and Ti_{35} samples shows uniform elongation. Thus, they do not have plasticity. In general, no clear elastic-plastic transition behavior is shown in any of the samples after any of the performed mechanical tests. Thus, the yield strength and elastic modulus were not calculated from them.

Tensile (119–256 MPa) maximum strengths from Table 3 were higher than those of cortical (77–98 MPa) and trabecular (25–55 MPa) bones [3]. Moreover, the TNZT alloys from this work showed higher tensile than Ti lattice structures with 40%–80% porosity for biomedical applications (25–210 MPa) [45]. The studied TNZT alloys also showed maximum bending strength (225–475 MPa) within the range of osteons (350–390 MPa) [46], which may encourage a low mechanical mismatch between the implant and the bone. However, stress state analyses are recommended to match the mechanical requirements of specific body part implants and those of the metallic biomaterial [3]. Regarding other P&S biomedical alloys from the literature, the studied TNZT of this work showed higher bending strength than Ti–In alloys (~300 MPa) [13] but lower than Ti–35Nb–5In (610 MPa) [32].

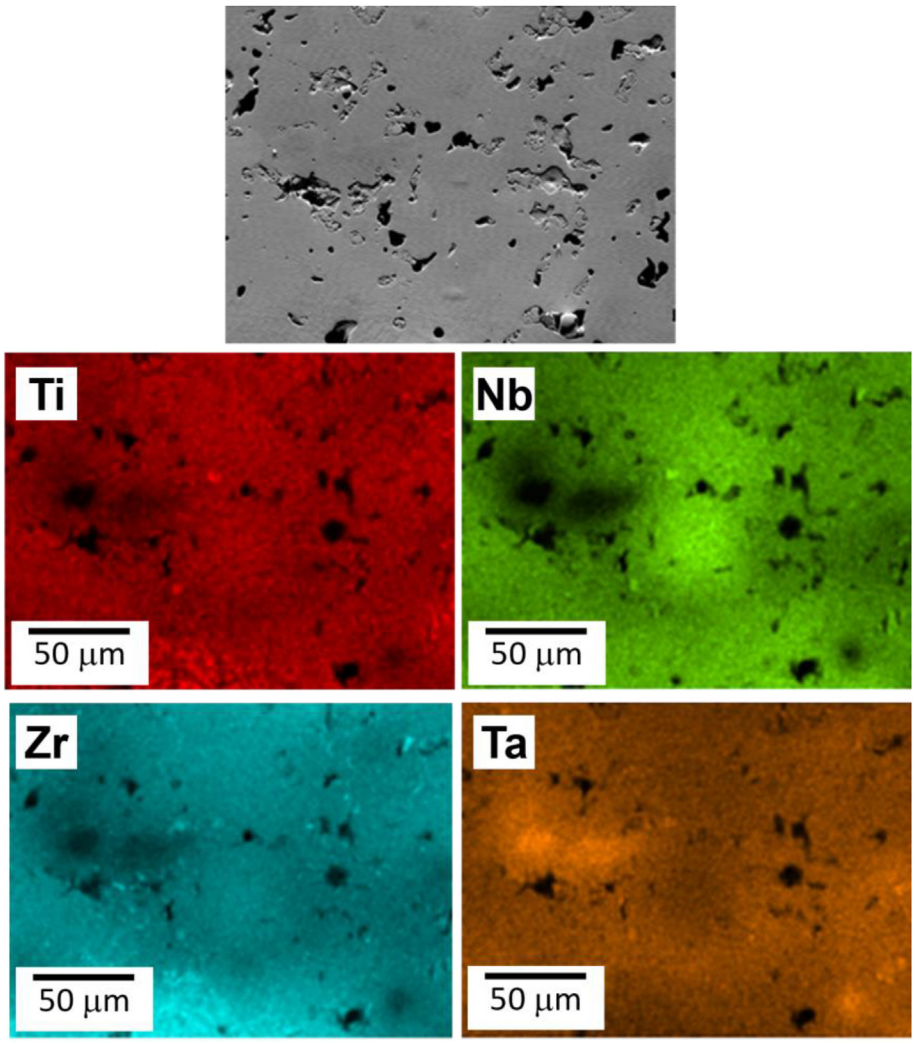

Fig. 3 – EDS mapping of the Ti_{25} sample. The chemical elements distribution showed similar tendencies on the samples Ti_{30} and Ti_{35}.

Fig. 5c shows the fracture mode of the Ti_{25} sample, which was selected as representative of the fracture behavior of the three studied samples. The typical characteristics of brittle fracture, such as cleavage and bright granular appearance, due to the lack of ductility can be observed in Fig. 5c.

Table 3 shows the average mechanical properties obtained from bending, tensile, microhardness, and IET tests. The increment of microhardness with the Ti content (and decreasing Ta content) agreed with the increment of US. The hardness of the three alloys (3.6–4.2 GPa) was above the reported for osteonal, interstitial, and trabecular bone regions (0.23–0.76 GPa) [33]. Besides, it was comparable to that of multiple Ti alloys designed for orthopedic purposes, such as Ti–6Al–4V (~2.8 GPa) [34], Ti–In (1.3–1.4 GPa) [13], and Ti–Nb–Mo alloys (1.8–2.8 GPa) [35].

The elastic modulus measured by IET in the TNZT alloys (83–90 GPa) was similar to the reported β-BCC-like Ti–Nb–Mo (64–96 GPa) [35] and Ti–35Nb alloys (94 GPa) [47]. The elastic modulus was also lower than other alloys for orthopedic implants, such as Ti–In (114–117 GPa) [13] and Ti–Zr (82–115 GPa) [48]. However, the elastic modulus of the TNZT alloys was higher than the human femur (<25 GPa [33]). Fig. 5d allows a better comparison of elastic moduli among reference materials, i.e., commercially pure Ti (CP–Ti), Ti–6Al–4V and human femur, as well as TNZT and porous biomedical alloys from the literature. From the above, the studied TNZT alloys meet the mechanical requirements for their use in orthopedic applications. The microstructure-mechanical performance relationship will be discussed later.

On the other hand, the possible multiple bond strengths due to variable atomic pairs in HEAs may not have a strong influence on the elastic moduli of the TNZT alloys compared to traditional alloys with a main element as matrix. The three studied alloys followed the expected trend of other TNZT alloys with similar Ti/Ta ratios (75–85 GPa) [49]. Moreover, those elastic moduli values are similar to those reported for Ti–Nb–Ta–Zr alloys with Ti matrix (55–91 GPa) [50,51]. Systematic studies with varying chemical compositions and bond energy measurements may be necessary to evaluate this phenomenon.

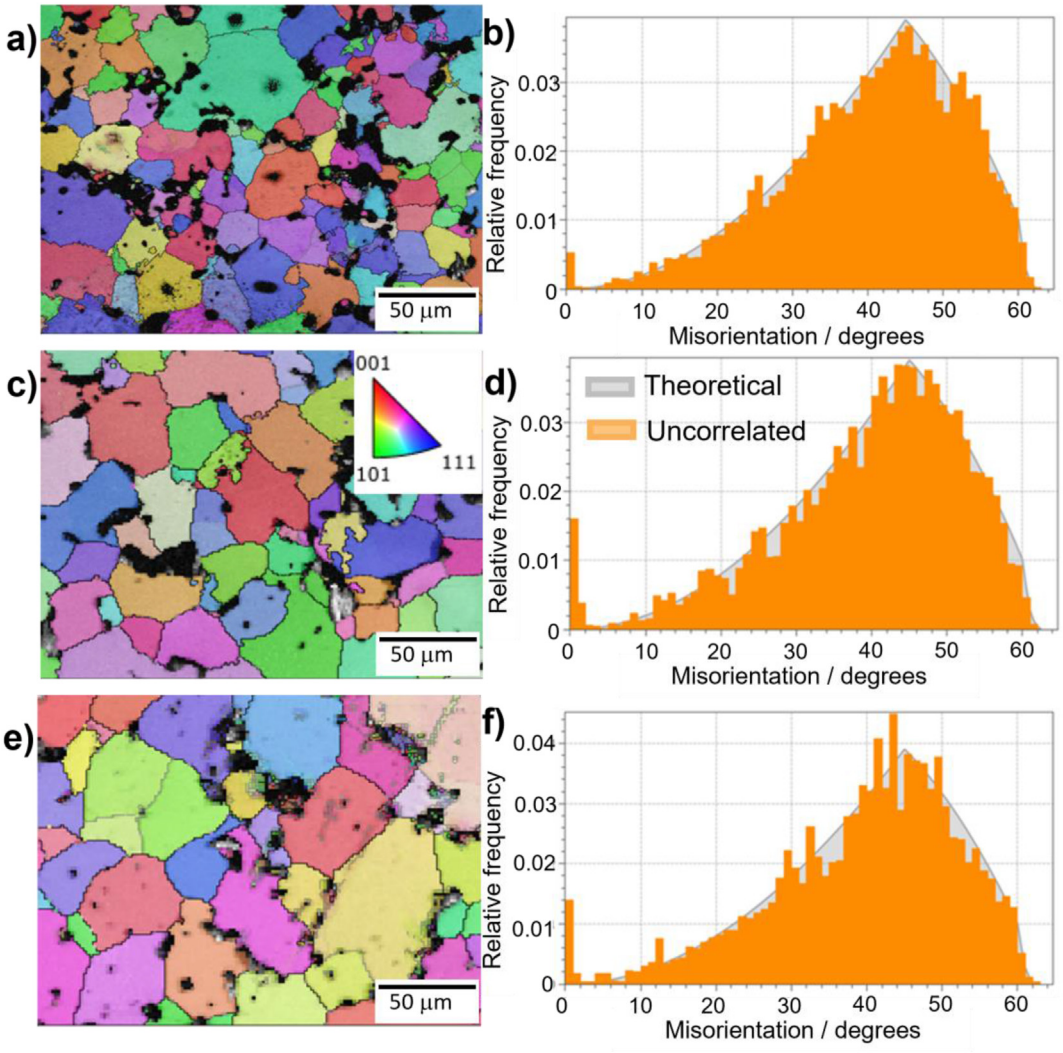

Fig. 4 – EBSD inverse pole figures (IPF) mapping with IPF color code inserted and misorientation angle distribution for the a,b) Ti_{25}, c,d) Ti_{30}, and e,f) Ti_{35} samples. Black regions in the EBSD mapping are attributed to porosity and/or no solution zones.

3.4. *Electrochemical evaluation*

The electrochemical behavior studied by OCP and PD polarization curves of the Ti_{25}, Ti_{30}, and Ti_{35} samples are shown in Fig. 6. The average corrosion parameters are shown in Table 4.

Fig. 6a and Table 4 show negative OCP values for the three studied samples, indicating an active ground-based alloy. The Ti_{25}, Ti_{30}, and Ti_{35} samples showed similar OCP tendencies, i.e., increment in the primary immersion stage up to about 3600, 1850, and 2900 s, respectively; then, it remained almost constant. Stable OCP values indicate the formation of a spontaneous surface passive layer.

Fig. 6b shows the potentiodynamic (PD) polarization curves of the Ti–35Nb–5In alloy. The three studied alloys exhibited similar electrochemical behavior described by; i) cathodic behavior and corrosion resistance region, ii) general corrosion region and starting of the anodic behavior, and iii) formation of a passive surface oxide layer. Besides, the Ti_{25} sample showed an increment of current density at a potential of around 0.9 V. The increase in current is commonly a consequence of active dissolution processes, which may involve pitting corrosion. The microstructure-electrochemical performance relationship will be discussed later.

On the other hand, the less negative E_{corr} of TNZT alloys (−0.280 to −0.369 V) compared to other P&S biomedical alloys, such as Ti–34Nb–6Sn [14] (−0.5 to −0.72 V), indicates a lower electrochemical activity of the former. This might be related to the forming of a more stable surface oxide film in the studied TNZT alloys.

3.5. *Ion release*

Metallic ion release rates are crucial for securing the low toxicity of biomaterials with potential implant applications, such as the TNZT alloys, to be introduced in *in-vivo* systems, such as the human body. Metallic ions can diffuse and

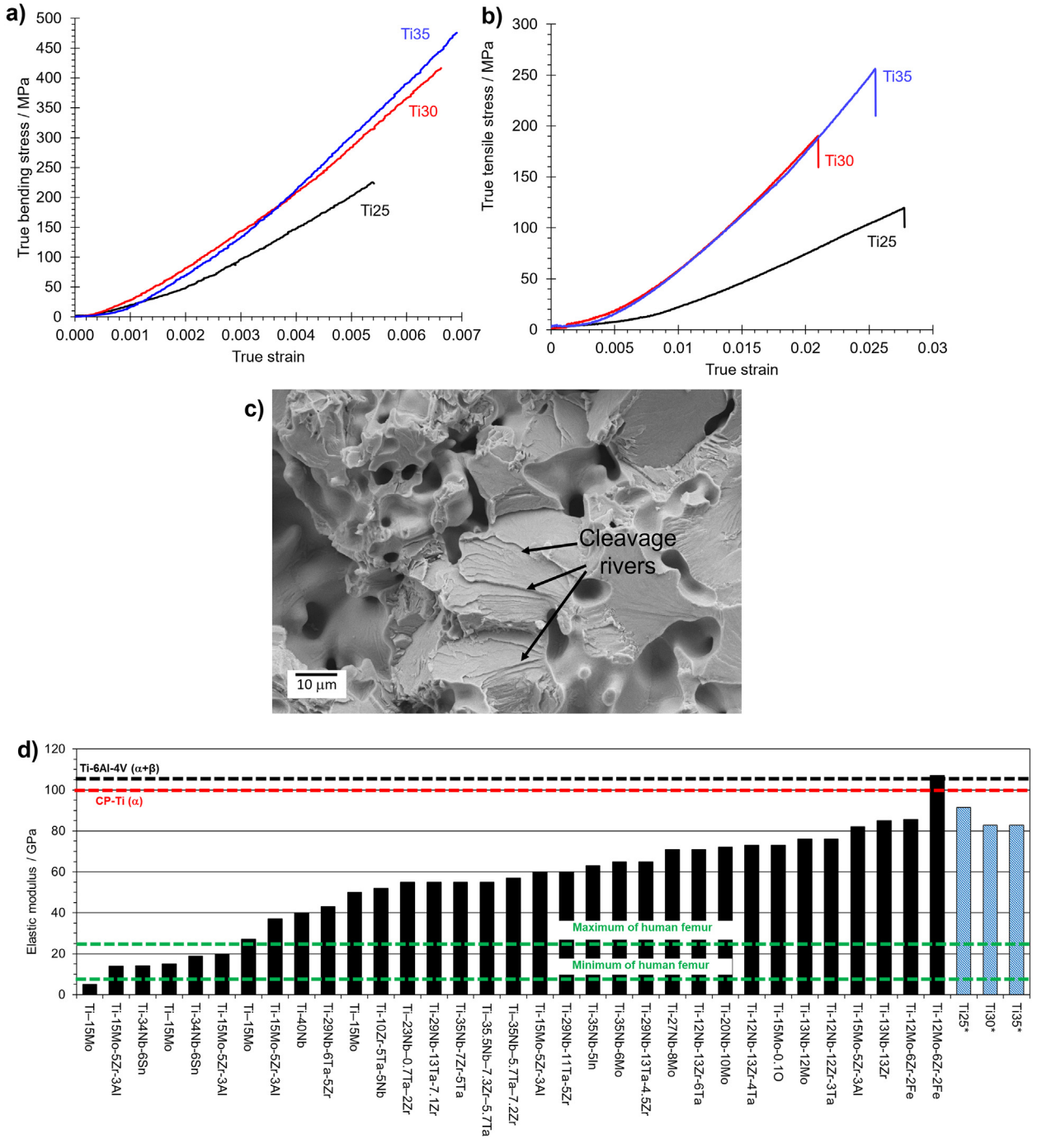

Fig. 5 – Stress-strain curves obtained by a) bending and b) tensile tests in the Ti_{25}, Ti_{30}, and Ti_{35} samples, as well as c) fracture micrograph after tensile test in the Ti_{25} sample and d) comparison of elastic moduli among TNZT alloys from this work (* blue columns) and from the literature and other porous BCC biomedical alloys [5,32–44].

accumulate in the human body and cause allergy and carcinoma at large concentrations [52]. Thus, a safe implant material should demonstrate metallic ion release rates well below the recommended dietary intake or reported toxicity levels. It is worth mentioning that because of the pitting behavior shown in Fig. 6, the Ti_{25} sample can be considered as not adequate for implant materials. Therefore, the ion release from this sample was not measured.

From Table 5, the ion release of the four constituent elements was below the harmful levels for the human body. The

Table 3 – Average mechanical properties obtained from microhardness, bending, tensile, and IET tests in the Ti_{25}, Ti_{30}, and Ti_{35} samples.

Sample	Bending		Tensile		Microhardness /HV	IET
	UBS/MPa	ε/%	UTS/MPa	ε/%		E/GPa
Ti_{25}	225.1 ± 15.8	0.53 ± 0.01	119.6 ± 1.7	2.15 ± 0.09	373.0 ± 6.3	91.39 ± 0.04
Ti_{30}	416.7 ± 16.6	0.66 ± 0.01	190.3 ± 15.7	1.53 ± 0.04	399.6 ± 8.4	82.78 ± 0.03
Ti_{35}	475.5 ± 24.7	0.76 ± 0.01	256.2 ± 16.9	2.08 ± 0.01	430.0 ± 7.4	82.84 ± 0.02

Ti^{3+} released from both Ti_{30} and Ti_{35} alloys was well below the limits of 10 ppm (10,000 μg L^{-1}) and 5 ppm (5000 μg L^{-1}), which inhibit and do not stimulate cell proliferation, respectively [53].

Moreover, the Nb release from 3.6 to 9.3 ng L^{-1} cm^{-2} h^{-1} (2.1102×10^{-5} to 5.4515×10^{-5} mM) are below the 0.5 and 5 mM of Nb^{5+} that induce DNA damage and <50% viability, i.e., the concentration at which 50% of healthy cells are alive [54]. The Nb release from the TNZT alloys is also below the non-toxic concentration of 172.0 μg L^{-1} [55].

Regarding Ta, the ion release values from 0.6 to 6.2 ng L^{-1} cm^{-2} h^{-1} were well below the 8000 mg kg^{-1} of tantalum oxide that has been proven as nontoxic after oral ingestion by rats [56]. The measured Ta concentration was also below the median lethal dose (LD_{50}, the dose required to kill 50% of a tested population) by oral administration of potassium tantalum fluoride and tantalum chloride of 2500 and 1900 mg kg^{-1}, respectively [56]. Remarkably, c on various cells in vitro systems [56].

For last, the concentrations of Zr ion release from 0.6 to 2.5 ng L^{-1} cm^{-2} h^{-1} were below the concentration necessary to cause 50% of the maximum possible effect (EC_{50}) of 4.3 mg L^{-1} and LC_{50} of 20 mg L^{-1} tested in fish [57]. The Zr release was also below the toxic concentrations from 1.3 to 2.5 mg L^{-1} in algae [57]. Besides, the Zr release from 0.6 to 2.5 ng L^{-1} cm^{-2} h^{-1} (3.5820×10^{-6} to 1.4925×10^{-5} mM) are below the 5 mM that induced <50% viability and DNA damage [54].

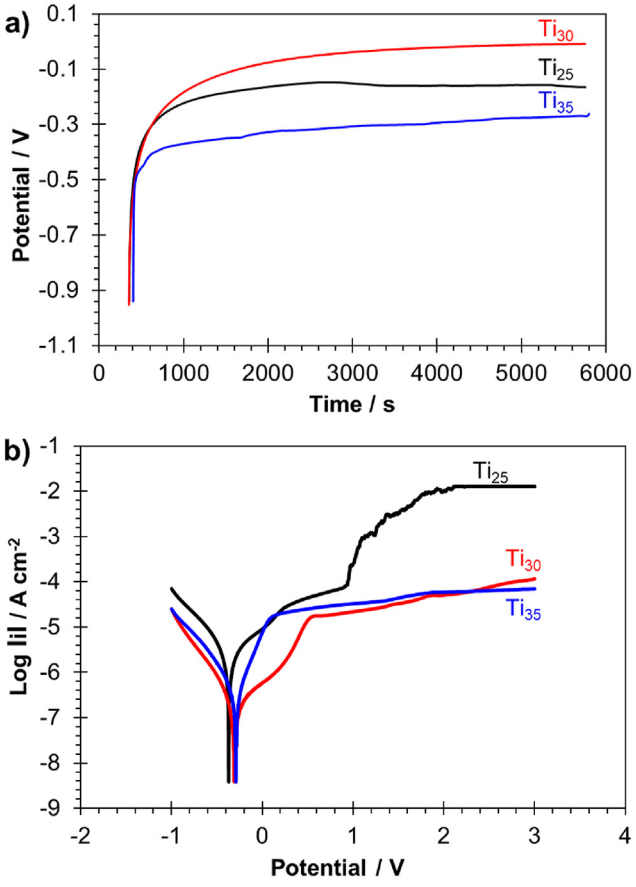

Fig. 6 – a) Open circuit potential (OCP) and b) potentiodynamic (PD) polarization curves with a single-layer circuit for the Ti_{25}, Ti_{30}, and Ti_{35} samples.

4. Discussion

4.1. *Microstructure-mechanical properties relationship*

The low ductility of the studied samples was suggested by the lack of uniform elongation in Fig. 5b. The low ductility may be related to various factors including i) the effect of porosity and other defects, ii) the presence of HCP phase, or iii) the atomic mismatch among alloying elements.

Porosity and pore size decreased the elongation in Ti–6Al–4V alloy [58]. Pores cause blocking of dislocation slip and heterogeneous deformation due to strain localization. This microstructural effect is not associated with the chemical composition or the crystalline structure. Thus, a similar effect may be expected for the TNZT alloys of this work, which porosity has been shown in the micrographs of Figs. 2 and 3.

Phase boundaries in the TNZT alloys could act as a dislocations obstacle and decreased their motion. From Fig. 7 can be seen that the elemental segregation shown in Fig. 3 corresponds to the distribution of BCC1 and BCC2 phases. In PM processes, the segregation arises typically in wider zones, as shown in Fig. 7. The phase map of Fig. 7 was done by the "TruePhase" procedure in AZtec software, which combines the information of Kikuchi bands orientation angles and EDS pixel-by-pixel analysis. The Ti_{25} sample was selected as representative of the phase distribution in Ti_{30} and Ti_{35} samples. In this way, Fig. 7 identifies the distribution of BCC1 (red zones), BCC2 (blue zones), and HCP (green zones) phases. In addition, the pores may decrease the dislocation mean free path, which reduces ductility.

Regarding crystalline structure effect, the HCP structure does not meet the criterion of at least five active slip systems for plastic deformation, i.e., plasticity. Besides, it is known that plasticity is mainly controlled by the crystalline structure

Table 4 – Electrochemical parameters from potentiodynamic (PD) curves of the studied Ti_{25}, Ti_{30}, and Ti_{35} alloys.

Alloy	OCP/V	E_{corr}/V	i_{corr}/μA cm^{-2}	R_p/kΩ cm^{-2}	C_r/μm $year^{-1}$
Ti_{25}	−0.29 ± 0.05	−0.37 ± 0.01	0.05 ± 0.01	53 ± 9	4.52
Ti_{30}	−0.23 ± 0.01	−0.29 ± 0.02	0.06 ± 0.02	423 ± 44	5.86
Ti_{35}	−0.20 ± 0.04	−0.28 ± 0.02	0.10 ± 0.03	258 ± 56	9.62

of metals and alloys [59]. However, the HCP content from 4 to 8 wt% in the studied TNZT alloys (Table 2), may not be sufficient to cause a significant effect on bulk mechanical properties. Near-BCC TNZT alloys with low HCP phase content have reported a clear elastic to plastic transition behavior with more than 30% strain to fracture during bending [60]. Therefore, the other mentioned factors may have a higher influence on the elastic behavior than the structure.

For last, the atomic radii differences among alloying elements in the TNZT alloys may promote low ductility. In fact, atomic radii mismatch, being a microstructural feature that causes lattice distortion, may act as a dislocations blocker to increase stress and reduce ductility [61]. Considering the atomic radius from the periodic table for Ti (147 p.m.), Nb (207 p.m.), Zr (160 p.m.), and Ta (220 p.m.), partial replacement of Ta for Ti may decrease the mismatch and improve ductility [62] and in general, modify the mechanical response of the alloy. Therefore, the high Ta content used in this work (15–25 wt%) may influence the elastic behavior of the alloys. In the cast conditions, it has been shown that partial replacement of Ta by Ti in Ti40–Zr25–Nb25–Ta10 and Ti45–Zr25–Nb25–Ta5 alloys considerably increased the ductility compared to the Ti25–Nb25–Zr25–Ta25, Ti30–Nb25–Zr25–Ta20, and Ti35–Nb25–Zr25–Ta15 alloys [62]. However, PM TNZT alloys with elemental segregation have shown a lack of ductility in the sample with the lowest Ta content (15 at.%) [63], but this cannot be confirmed in PM samples due to the inherent porosity that impedes the ductility.

4.2. *Effect of microstructure on electrochemical properties and ion release*

Fig. 6b showed a transpassive region in Ti_{25} sample when potential increases, while the Ti_{30} and Ti_{35} samples remain at stable current density with higher potential. The transpassive region in the Ti_{25} sample is a suggestion of dissolution of the alloy and ion release. From the above, higher ion release rates can be expected from the Ti_{25} sample (especially in electrochemical environments) compared to the Ti_{30} and Ti_{35} samples.

The transpassive region in the Ti_{25} alloy may be related to defects, such as pores, chemical or topological heterogeneities, as well as crystallographic texture, which may provide conditions for local corrosion. Besides, galvanic pairs may be discarded due to the nearly random crystallographic orientation (Fig. 4a) but may be present due to surface energy differences among phases. Thus, the local chemical and morphological heterogeneities in the Ti_{25} alloy can be explained by the porosity, chemical segregation, and multiphase microstructures shown in Figs. 2, 3 and 7. The occurrence of pitting corrosion may decrease the electrochemical stability and feasibility of the Ti_{25} sample as biomedical implant material.

Regarding the corrosion rates at ion release testing (Table 5), the higher value of the Ti_{35} compared to the Ti_{30} agreed with its also higher electrochemical corrosion rate shown in Table 4. A higher corrosion rate in the sample with higher Ti content was expected from the higher electronegativity of Ti (~2.0 [64]) compared to Ta (~1.3 [65]). Thus, the preferred dissolution of Ti, which is also the matrix in the Ti_{35} sample, could be responsible for the more accelerated dissolution of the alloy. The preferred dissolution of Ti is also related to the higher dissolution of the Ti- and Zr-enriched HCP phase (Fig. 1). As the HCP-phase content increased in the Ti_{35} sample with respect to the Ti_{30} sample (Table 2), the higher ion release of Ti and Zr from the first one was expected. Despite the preferred dissolution of Ti, the electrochemical corrosion rates from 4.5 to 9.6 μm $year^{-1}$ of the three studied TNZT alloys (Table 4) can be classified as very stable [66].

Comparisons with other TNZT alloys tested at similar conditions are shown in Fig. 8. Reported cast TNZT alloys [60] showed lower levels of ion release compared to those produced by additive manufacturing (AM [67]) and the powder metallurgy processed-alloys of this work. This phenomenon is explained by the highest compaction of dense materials, such as cast, compared to those produced by bottom-up methods.

Regarding the reported TNZT alloys by AM [67] and the Ti_{30} sample of this work, the Zr release from the last one was lower despite its higher content on the alloy (Fig. 8). Ta release from the Ti_{30} sample was between the reported levels from AM-produced alloys. However, the Ti_{35} sample showed a different tendency by a higher Zr and Ti release, as well as a lower Ta release compared to those from the AM-produced alloys. This behavior can be related to the preferred dissolution of Ti compared to the other alloying elements. While the higher dissolution of Zr and lower of Ta could be related to the wt.% in the alloy.

Table 5 – Average metallic ion release and corrosion rate from the Ti_{30} and Ti_{35} alloys.

Sample	Ion release rate/ng L^{-1} cm^{-2} h^{-1}				Corrosion rate /mg dm^{-2} day^{-1}	Corrosion rate /μm $year^{-1}$
	Ti	Nb	Zr	Ta		
Ti_{30}	2.5 ± 1.0	9.3 ± 4.3	0.6 ± 0.1	6.2 ± 2.0	$2.2 \times 10^{-7} \pm 2.8 \times 10^{-8}$	0.9 ± 0.1
Ti_{35}	5.4 ± 0.0	3.6 ± 0.0	2.5 ± 0.2	0.6 ± 0.1	$1.4 \times 10^{-7} \pm 1.8 \times 10^{-8}$	1.1 ± 0.1

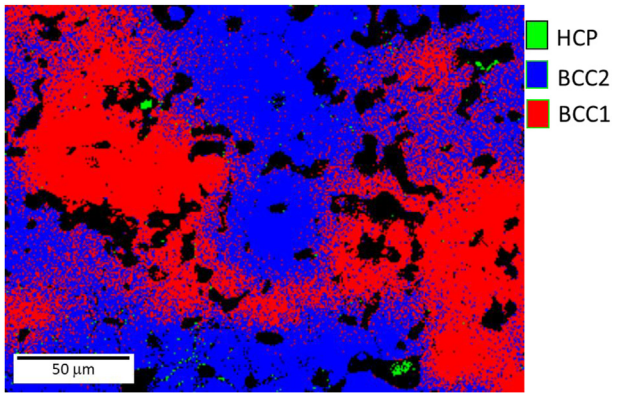

Fig. 7 – Phase segregation in the Ti_{25} sample.

Considering that the TNZT alloys were mainly designed for biomedical applications, their corrosion rates will be compared with other feasible metallic implant materials from the literature. Fig. 8b shows the comparison of corrosion rate after ion release testing of Ti_{30} and Ti_{35} samples with other porous Ti alloys tested at similar media, i.e., Fusayama or modified Ringer-Hartmann artificial saliva [13–15,34,35]. Ti_{30} and Ti_{35} samples showed corrosion rates similar to those of porous Ti–6Al–4V, but higher than the Ti–Nb–Mo, Ti–In, and Ti–Nb–In systems. However, TNZT alloys are highly advantageous in terms of non-toxicity, while Mo, In, Al, and V have shown potential allergenic, carcinogenic, genotoxic, cytotoxic, or mutagenic effects [22,68–70].

From the above, electrochemical corrosion rates can be considered as stable. However, the Ti_{25} sample may have reduced feasibility for implant materials due to the occurrence of pitting. The ion release rates from the TNZT alloys met the non-toxicity requirement for their use as biomedical implants. However, future in-vivo testing may be necessary to confirm this statement.

5. Conclusions

The microstructural, mechanical, and electrochemical performance of porous Ti_{25}–Nb_{25}–Zr_{25}–Ta_{25}, Ti_{30}–Nb_{25}–Zr_{25}–Ta_{20}, and Ti_{35}–Nb_{25}–Zr_{25}–Ta_{15} (TNZT) alloys was evaluated. The Ti_{30}–Nb_{25}–Zr_{25}–Ta_{20} and Ti_{35}–Nb_{25}–Zr_{25}–Ta_{15} alloys were demonstrated as feasible candidates for biomedical implant applications. This conclusion was based on the following specific findings.

(1) The microstructure of the three TNZT alloys consisted of nearly-equiaxed BCC phases and low content of HCP

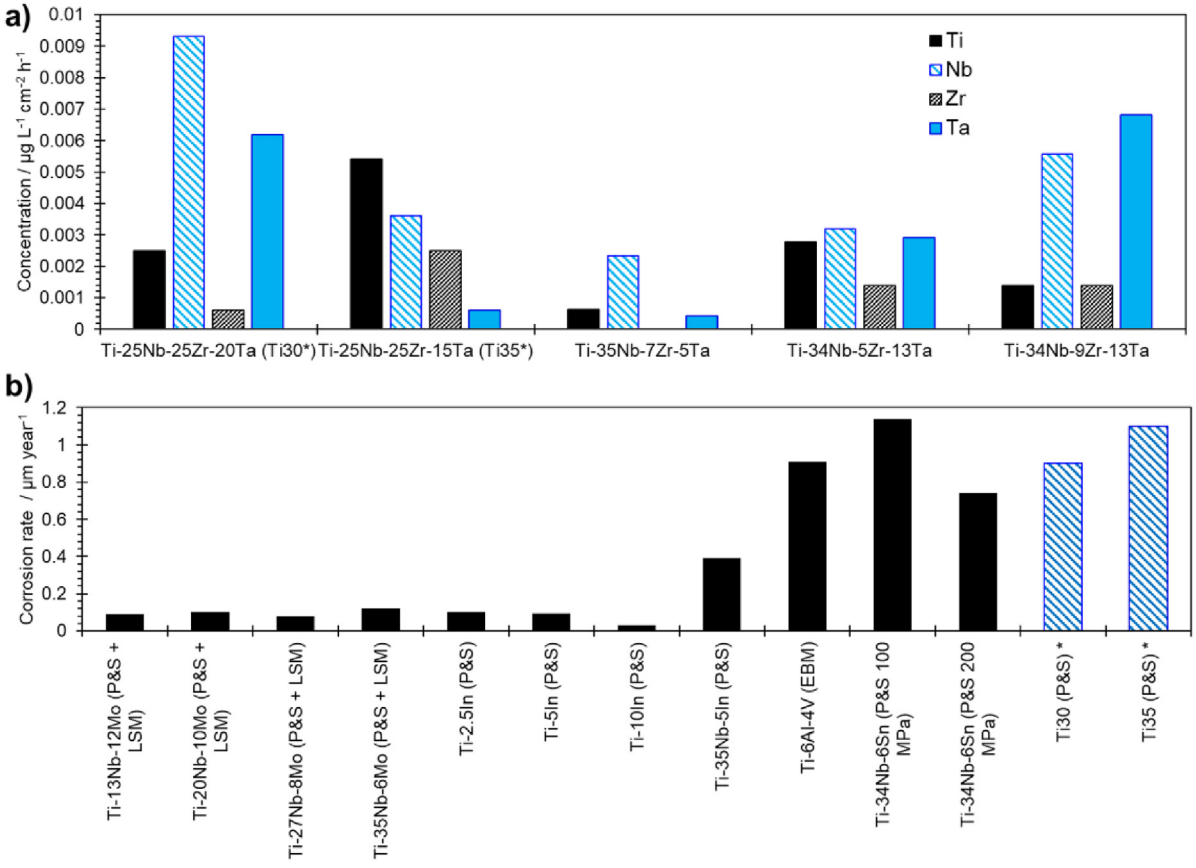

Fig. 8 – Comparison of properties among biomedical alloys from the literature and the TNZT alloys of this work (*). a) Ion release among different TNZT alloys, including the Ti_{30} and Ti_{35} samples by P&S, Ti–35Nb–7Zr–5Ta prepared by casting [60], Ti–34Nb–5Zr–13Ta and Ti– 34Nb–9Zr–13Ta prepared by selective laser melting (SLM) [67]. b) Corrosion rate after ion release testing of various porous Ti biomedical alloys tested at artificial saliva [13–15,34,35].

phase. The correlated and uncorrelated misorientation profiles suggested random crystallographic texture on the BCC matrix of the three alloys.

(2) The elastic modulus of the TNZT alloys was around 3 times higher (83–90 GPa) than the reported for the human femur but smaller than other reported implant Ti alloys. The hardness (3.6–4.2 GPa) was also higher than the reported for the human bone.

(3) The electrochemical corrosion rate (4.5–9.6 μm year^{-1}) can be considered very stable. The lower Ti content (sample Ti_{25}–Nb_{25}–Zr_{25}–Ta_{25} with the highest Ta content) showed local corrosion due to the probable galvanic pairs formed at pores, chemical, and multiphase heterogeneities. Due to pitting, the sample Ti_{25}–Nb_{25}–Zr_{25}–Ta_{25} could have reduced feasibility as a biomedical implant compared to the Ti_{30}–Nb_{25}–Zr_{25}–Ta_{20} and Ti_{35}–Nb_{25}–Zr_{25}–Ta_{15} samples.

(4) The Ti, Nb, Zr, and Ta releases (Ti: 2.5–5.4; Nb: 3.6–9.3; Zr: 0.6–2.5; and Ta: 0.6–6.2 ng L^{-1} cm^{-2} h^{-1}) were below the reported toxic levels for human or animal health. The HCP phase was preferentially dissolved compared to the BCC phases in the studied TNZT alloys.

Data availability

The raw data related to this manuscript would be made available on request.

Declaration of competing interest

The authors declare that they have no known competing financial interests or personal relationships that could have appeared to influence the work reported in this paper.

Acknowledgments

V. A. acknowledges the funding from the Spanish Ministerio de Ciencia, Innovación y Universidades with project RTI2018-097810-B-I00, and the European Commission via Fondo Europeo de Desarrollo Regional (FEDER). G. G. acknowledges UNAM-DGAPAPASPA program for funding the sabbatical year at the UPV, as well as Programa de Apoyo a Proyectos de Investigacion e Innovacion Tecnologica (PAPIIT)-UNAM under grant number IN102321. L. R. R. acknowledges the funding from Programa de Apoyo a la Investigación y el Posgrado (PAIP)-UNAM. A.L.V. acknowledges FAPESP for financial support in his internship at UPV (grant 2021/11537–1).

REFERENCES

[1] Elani HW, Starr JR, Da Silva JD, Gallucci GO. Trends in dental implant use in the U.S., 1999–2016, and projections to 2026. J Dent Res 2018;97:1424–30. https://doi.org/10.1177/0022034518792567.

[2] Klug A, Gramlich Y, Rudert M, Drees P, Hoffmann R, Weißenberger M, et al. The projected volume of primary and revision total knee arthroplasty will place an immense burden on future health care systems over the next 30 years. Knee Surg Sports Traumatol Arthrosc 2021;29:3287–98. https://doi.org/10.1007/s00167-020-06154-7.

[3] Guo L, Ataollah Naghavi S, Wang Z, Nath Varma S, Han Z, Yao Z, et al. On the design evolution of hip implants: a review. Mater Des 2022;216:110552. https://doi.org/10.1016/j.matdes.2022.110552.

[4] Cui YW, Chen LY, Chu YH, Zhang L, Li R, Lu S, et al. Metastable pitting corrosion behavior and characteristics of passive film of laser powder bed fusion produced Ti–6Al–4V in NaCl solutions with different concentrations. Corrosion Sci 2023;215:111017. https://doi.org/10.1016/j.corsci.2023.111017.

[5] Mohammed MT, Khan ZA, Siddiquee AN. Beta titanium alloys: the lowest elastic modulus for biomedical applications: a review. Int J Chem Nucl Metall Mater Eng 2014;8:726–31.

[6] Anene FA, Aiza Jaafar CN, Zainol I, Azmah Hanim MA, Suraya MT. Biomedical materials: a review of titanium based alloys. Proc Inst Mech Eng Part C J Mech Eng Sci 2021;235:3792–805. https://doi.org/10.1177/0954406220967694.

[7] Zhang R, Zhao S, Ding J, Chong Y, Jia T, Ophus C, et al. Short-range order and its impact on the CrCoNi medium-entropy alloy. Nature 2020;581:283–7. https://doi.org/10.1038/s41586-020-2275-z.

[8] Ching WY, San S, Brechtl J, Sakidja R, Zhang M, Liaw PK. Fundamental electronic structure and multiatomic bonding in 13 biocompatible high-entropy alloys. npj Comput Mater 2020;6:1–10. https://doi.org/10.1038/s41524-020-0321-x.

[9] Nasibi S, Alimohammadi K, Bazli L, Eskandarinezhad S, Mohammadi A, Sheysi N. TZNT alloy for surgical implant applications: a systematic review. J Compos Compd TZNT 2020;2:62–8. https://doi.org/10.29252/jcc.2.2.1.

[10] Bram Dr M, Ebel Dr T, Wolff M, Cysne Barbosa Dr AP, Tuncer Dr N. Applications of powder metallurgy in biomaterials. Advances in powder metallurgy, Woodhead Publishing; 2013, p. 520–554. https://doi.org/10.1533/9780857098900.4.520.

[11] Ponader S, Von Wilmowsky C, Widenmayer M, Lutz R, Heinl P, Körner C, et al. In vivo performance of selective electron beam-melted Ti-6Al-4V structures. J Biomed Mater Res, Part A 2010;92:56–62. https://doi.org/10.1002/jbm.a.32337.

[12] Goia TS, Violin KB, Yoshimoto M, Bressiani JC, Bressiani AHA. Osseointegration of titanium alloy macroporous implants obtained by PM with addition of gelatin. Adv Sci Technol 2010;76:259–63. https://doi.org/10.4028/www.scientific.net/ast.76.259.

[13] Romero-Resendiz L, Gómez-Sáez P, Vicente-Escuder A, Amigó-Borrás V. Development of Ti-In alloys by powder metallurgy for application as dental biomaterial. J Mater Res Technol 2021;11:1719–29. https://doi.org/10.1016/j.jmrt.2021.02.014.

[14] Correa-Rossi M, Romero-Resendiz L, Leal-Bayerlein D, Garcia-Alves AL, Segovia-l F, Amigo V. Mechanical, corrosion, and ion release studies of Ti-34Nb-6Sn alloy with comparable to the bone elastic modulus by powder metallurgy method. Powders 2022;1:3–17. https://doi.org/10.3390/powders1010002.

[15] Romero-Resendiz L, Rossi MC, Segui-Esquembre C, Amigo-Borras V. Development of a porous Ti-35Nb-5In alloy with low elastic modulus for biomedical implants. J o f Mater Res Technol 2023;22:1151–64. https://doi.org/10.1016/j.jmrt.2022.12.011.

[16] Committee AIH. Powder metal technologies and applications, vol. 7. ASM International Handbook Committee; 1998.

[17] Gonçalves de Oliveira T, Valim Fagundes D, Capellato P, Sachs D. Araujo Pinto daSilva A.A. A review of biomaterials based on high-entropy alloys. Metals 2022;12:1940. https://doi.org/10.3390/met12111940.
[18] Yokota K, Bahador A, Shitara K, Umeda J, Kondoh K. Mechanisms of tensile strengthening and oxygen solid solution in single β-phase Ti-35 at.%Ta+O alloys. Mater Sci Eng, A 2021;802:140677. https://doi.org/10.1016/j.msea.2020.140677.
[19] Ibrahim MK, Hamzah E, Saud SN, Nazim EM, Iqbal N, Bahador A. Effect of Sn additions on the microstructure, mechanical properties, corrosion and bioactivity behaviour of biomedical Ti–Ta shape memory alloys. J Therm Anal Calorim 2018;131:1165–75. https://doi.org/10.1007/s10973-017-6636-2.
[20] Homma T, Arafah A, Haley D, Nakai M, Niinomi M, Moody MP. Effect of alloying elements on microstructural evolution in oxygen content controlled Ti-29Nb-13Ta-4.6Zr (wt%) alloys for biomedical applications during aging. Mater Sci Eng, A 2018;709:312–21. https://doi.org/10.1016/j.msea.2017.10.018.
[21] Kopova I, Stráský J, Harcuba P, Landa M, Janeček M, Bačákova L. Newly developed Ti-Nb-Zr-Ta-Si-Fe biomedical beta titanium alloys with increased strength and enhanced biocompatibility. Mater Sci Eng C 2016;60:230–8. https://doi.org/10.1016/j.msec.2015.11.043.
[22] Sidhu SS, Singh H, Gepreel MAH. Recent development in beta titanium alloys for biomedical applications. Mater Sci Eng C 2021;121:111661–77. https://doi.org/10.1016/j.msec.2020.111661.
[23] Lutterotti L. Maud: a Rietveld analysis program designed for the internet and experiment integration. Acta Crystallogr Sect A Found Crystallogr 2000;56:s54. https://doi.org/10.1107/s0108767300021954. –s54.
[24] ASM Handbook Committee. ASM handbook. Corrosion: fundamentals, testing, and protection, 13A. ASM International; 2003.
[25] Loke C, Lee J, Sander S, Mei L, Farella M. Factors affecting intra-oral pH - a review. J Oral Rehabil 2016;43:778–85. https://doi.org/10.1111/joor.12429.
[26] Goldstein LS, Dewhirst MW, Repacholi M, Kheifets L. Summary, conclusions and recommendations: adverse temperature levels in the human body. Int J Hyperther 2003;19:373–84. https://doi.org/10.1080/0265673031000090701.
[27] Bahador A, Kariya S, Umeda J, Hamzah E, Kondoh K. Tailoring microstructure and properties of a superelastic Ti–Ta alloy by incorporating spark plasma sintering with thermomechanical processing. J Mater Eng Perform 2019;28:3012–20. https://doi.org/10.1007/s11665-019-04061-8.
[28] Bahador A, Hamzah E, Kondoh K, Abu Bakar TA, Yusof F, Imai H, et al. Effect of deformation on the microstructure, transformation temperature and superelasticity of Ti–23 at% Nb shape-memory alloys. Mater Des 2017;118:152–62. https://doi.org/10.1016/j.matdes.2016.12.048.
[29] Ansel D, Thibon I, Boliveau M, Debuigne J. Interdiffusion in the body cubic centered β-phase of TA-TI alloys. Acta Mater 1998;46:423–30. https://doi.org/10.1016/S1359-6454(97)00272-3.
[30] Senkov ON, Chakoumakos BC, Jonas JJ, Froes FH. Effect of temperature and hydrogen concentration on the lattice parameter of beta titanium. Mater Res Bull 2001;36:1431–40. https://doi.org/10.1016/S0025-5408(01)00604-3.
[31] Mackenzie JK. Second paper on statistics associated with the random disorientation of cubes. Biometrika 1958;45:229–40. https://doi.org/10.2307/2333253.
[32] Romero-Resendiz L, Rossi MC, Seguí-Esquembre C, Amigó-Borrás V. Development of a porous Ti–35Nb–5In alloy with low elastic modulus for biomedical implants. J Mater Res Technol 2023;22:1151–64. https://doi.org/10.1016/j.jmrt.2022.12.011.
[33] Zysset PK, Guo XE, Ho CE, Moore KE, Goldstein SA. Elastic modulus and hardness of cortical and trabecular bone lamellae measured by nanoindentation in the human femur. J Biomech 1999;32:1005–12. https://doi.org/10.1016/S0021-9290(99)00111-6Get.
[34] Romero-Resendiz L, Rossi MC, Alvarez A, García-García A, Milian L, Tormo-Mas MA, et al. Microstructural, mechanical , electrochemical, and biological studies of an electron beam melted Ti-6Al-4V alloy. Mater Today Commun 2022;31:103337–51. https://doi.org/10.1016/j.mtcomm.2022.103337.
[35] Tendero I, Rossi MC, Viera M, Amado JM, Tobar MJ, Vicente Á, et al. Laser surface modification in Ti-xNb-yMo alloys prepared by powder metallurgy. Metals 2021;11:367–87. https://doi.org/10.3390/met11020367.
[36] Zhou L, Chen J, Huang WY, Ren Y, Niu Y, Yuan T. Effects of Ta content on phase transformation in selective laser melting processed Ti-13Nb-13Zr alloy and its correlation with elastic properties. Vacuum 2021;183:109798. https://doi.org/10.1016/j.vacuum.2020.109798.
[37] Min X, Bai P, Emura S, ji X, Cheng C, Jiang B, et al. Effect of oxygen content on deformation mode and corrosion behavior in β-type Ti-Mo alloy. Mater Sci Eng, A 2017;684:534–41. https://doi.org/10.1016/j.msea.2016.12.062.
[38] Duan R, Li S, Cai B, Zhu W, Ren F, Attallah MM. A high strength and low modulus metastable β Ti-12Mo-6Zr-2Fe alloy fabricated by laser powder bed fusion in-situ alloying. Addit Manuf 2021;37:101708. https://doi.org/10.1016/j.addma.2020.101708.
[39] Elias CN, Fernandes DJ, Resende CRS, Roestel J. Mechanical properties, surface morphology and stability of a modified commercially pure high strength titanium alloy for dental implants. Dent Mater 2015;31:e1–13. https://doi.org/10.1016/j.dental.2014.10.002.
[40] Li YH, Chen RB, xia Qi G, Wang ZT, Deng ZY. Powder sintering of porous Ti-15Mo alloy from TiH2 and Mo powders. J Alloys Compd 2009;485:215–8. https://doi.org/10.1016/j.jallcom.2009.06.003.
[41] Nomura N, Kohama T, Oh IH, Hanada S, Chiba A, Kanehira M, et al. Mechanical properties of porous Ti-15Mo-5Zr-3Al compacts prepared by powder sintering. Mater Sci Eng C 2005;25:330–5. https://doi.org/10.1016/j.msec.2005.04.001.
[42] Correa-Rossi M, Romero-Resendiz L, Leal-Bayerlein D, Garcia-Alves A, Segovia-López F, Amigó-Borrás V. Mechanical, corrosion, and ion release studies of Ti-34Nb-6Sn alloy with comparable to the bone elastic modulus by powder metallurgy method. Powders 2022;1:3–17. https://doi.org/10.3390/powders1010002.
[43] Aydogmus T, Al-Zangana NJF, Kelen F. Processing of β-type biomedical Ti74Nb26 alloy by combination of hot pressing and high temperature sintering. Konya J Eng Sci 2020;8:269–81. https://doi.org/10.36306/konjes.587790.
[44] Zhang LC, Chen LY. A review on biomedical titanium alloys: recent progress and prospect. Adv Eng Mater 2019;21:1–29. https://doi.org/10.1002/adem.201801215.
[45] Dumas M, Terriault P, Brailovski V. Modelling and characterization of a porosity graded lattice structure for additively manufactured biomaterials. Mater Des 2017;121:383–92. https://doi.org/10.1016/j.matdes.2017.02.021.
[46] Ascenzi A, Baschieri P, Benvenuti A. The bending properties of single osteons. J Biomech 1990;23:763–71. https://doi.org/10.1016/0021-9290(90)90023-V.
[47] Cremasco A, Ferreira I, Caram R. Effect of heat treatments on mechanical properties and fatigue resistance of Ti-35Nb

alloy used as biomaterial. Mater Sci Forum 2010;636–637:68–75. https://doi.org/10.4028/www.scientific.net/MSF.636-637.68.
[48] Amigó-Mata A, Haro-Rodriguez M, Vicente-Escuder Á, Amigó-Borrás V. Development of Ti–Zr alloys by powder metallurgy for biomedical applications. Powder Metall 2022;65:31–8. https://doi.org/10.1080/00325899.2021.1943182.
[49] Colombo G. The effect of equal channel angular extrusion (ECAE) and boron additions on the mechanical properties of a biomedical Ti-Nb-Zr-Ta (TNZT) alloy. St. Louis: Washington University; 2010.
[50] Mao C, Yu W, Jin M, Wang Y, Shang X, Lin L, et al. Bioactive Materials Mechanobiologically optimized Ti − 35Nb − 2Ta − 3Zr improves load transduction and enhances bone remodeling in tilted dental implant therapy. Bioact Mater 2022;16:15–26. https://doi.org/10.1016/j.bioactmat.2022.03.005.
[51] Zhang T, Wei D, Lu E, Wang W, Wang K, Li X, et al. Microstructure evolution and deformation mechanism of α+β dual-phase Ti-xNb-yTa-2Zr alloys with high performance. J Mater Sci Technol 2022;131:68–81. https://doi.org/10.1016/j.jmst.2022.04.052.
[52] Hanawa T. Metal ion release from metal implants. Mater Sci Eng C 2004;24:745–52. https://doi.org/10.1016/j.msec.2004.08.018.
[53] Liao H, Wurtz T, Li J. Influence of titanium ion on mineral formation and properties of osteoid nodules in rat calvaria cultures. J Biomed Mater Res 1999;47:220–7.
[54] Caicedo M, Jacobs JJ, Reddy A, Hallab NJ. Analysis of metal ion-induced DNA damage, apoptosis, and necrosis in human (Jurkat) T-cells demonstrates Ni2+ and V3+ are more toxic than other metals: Al3+, Be2+, Co2+, Cr 3+, Cu2+, Fe3+, Mo5+, Nb 5+, Zr2+. J Biomed Mater Res, Part A 2008;86:905–13. https://doi.org/10.1002/jbm.a.31789.
[55] Li Y, Wong C, Xiong J, Hodgson P, Wen C. Cytotoxicity of titanium and titanium alloying elements. J Dent Res 2010;89:493–7. https://doi.org/10.1177/0022034510363675.
[56] Bard Allen J, Parson Roger, Jordan Joseph. Vanadium, niobium, and tantalum. En standard Potentials in aqueous solution. 507-538. Routledge; 2017. https://doi.org/10.1201/9780203738764.
[57] Couture P, Blaise C, Cluis D, Bastien C. Zirconium toxicity assessment using bacteria, algae and fish assays. Water Air Soil Pollut 1989;47:87–100. https://doi.org/10.1007/BF00469000.
[58] Kumar P, Chandran KSR. Strength–ductility property maps of powder metallurgy (PM) Ti-6Al-4V alloy: a critical review of processing-structure-property relationships. Metall Mater Trans A Phys Metall Mater Sci 2017;48:2301–19. https://doi.org/10.1007/s11661-017-4009-x.
[59] Zhu T, Wu X. Heterostructured materials. Prog Mater Sci 2023;131:101019. https://doi.org/10.1016/j.pmatsci.2022.101019.
[60] Rossi MC, Ventura BN, Milián L, Escuder AV, Borrás VA. Study of electrochemical and biological characteristics of as-cast Ti-Nb-Zr-Ta system based on its microstructure. Metals 2022;12. https://doi.org/10.3390/met12030476.
[61] Nguyen VT, Qian M, Shi Z, Song T, Huang L, Zou J. Compositional design of strong and ductile (tensile) Ti-Zr-Nb-Ta medium entropy alloys (MEAs) using the atomic mismatch approach. Mater Sci Eng, A 2019;742:762–72. https://doi.org/10.1016/j.msea.2018.11.054.
[62] Nguyen VT. Equiatomic and non-equiatomic Ti-Zr-Nb-Ta refractory medium entropy alloys. University of Queensland; 2019.
[63] Xiang T, Du P, Cai Z, Li K, Bao W, Yang X, et al. Phase-tunable equiatomic and non-equiatomic Ti-Zr-Nb-Ta high-entropy alloys with ultrahigh strength for metallic biomaterials. J Mater Sci Technol 2022;117:196–206. https://doi.org/10.1016/j.jmst.2021.12.014.
[64] Li K, Xue D. Estimation of electronegativity values of elements in different valence states. J Phys Chem A 2006;110:11332–7. https://doi.org/10.1021/jp062886k.
[65] Mann JB, Meek TL, Knight ET, Capitani JF, Allen LC. Configuration energies of the d-block elements. J Am Chem Soc 2000;122:5132–7. https://doi.org/10.1021/ja9928677.
[66] Yang J, Yang H, Yu H, Wang Z, Zeng X. Corrosion behavior of additive manufactured Ti-6Al-4V alloy in NaCl solution. Metall Mater Trans A Phys Metall Mater Sci 2017;48:3583–93. https://doi.org/10.1007/s11661-017-4087-9.
[67] Kong W, Cox SC, Lu Y, Villapun V, Xiao X, Ma W, et al. The influence of zirconium content on the microstructure, mechanical properties, and biocompatibility of in-situ alloying Ti-Nb-Ta based β alloys processed by selective laser melting laser melting. Mater Sci Eng C 2021:131. https://doi.org/10.1016/j.msec.2021.112486.
[68] Castronovo FP, Wagner HN. Factors affecting the toxicity of the element indium. Br J Exp Pathol 1871;52:543. https://doi.org/10.1136/vr.94.20.456.
[69] Nakajima M, Usami M, Nakazawa K, Arishima K, Yamamoto M. Developmental toxicity of indium: embryotoxicity and teratogenicity in experimental animals. Congenital Anom 2008;48:145–50. https://doi.org/10.1111/j.1741-4520.2008.00197.x.
[70] Tanaka A, Hirata M, Kiyohara Y, Nakano M, Omae K, Shiratani M, et al. Review of pulmonary toxicity of indium compounds to animals and humans. Thin Solid Films 2010;518:2934–6. https://doi.org/10.1016/j.tsf.2009.10.123.